Title: Low variability, snowmelt runoff inhibits coupling of climate, tectonics, and topography in the Greater Caucasus

---

Author and Affiliations:
Adam M. Forte[1], Joel S. Leonard[2], Matthew W. Rossi[3], Kelin X. Whipple[2], Arjun M. Heimsath[2], Lasha Sukhishvili[4], Tea Godoladze[4], Fakhraddin Kadirov[5]

[1]Department of Geology & Geophysics, Louisiana State University, Baton Rouge, LA, USA
[2]School of Earth and Space Exploration, Arizona State University, Tempe, AZ, USA
[3]Earth Lab, Cooperative Institute for Research in Environmental Sciences (CIRES), University of Colorado, Boulder, CO, USA
[4]Institute of Earth Sciences and National Seismic Monitoring Center, Ilia State University, Tbilisi, Georgia
[5]Institute of Geology and Geophysics of Azerbaijan National Academy of Sciences, Baku, Azerbaijan

Corresponding Author: Adam M. Forte (aforte8@lsu.edu)
ORCID ID: 0000-0003-4515-7792
Twitter Handle: @AdamForte83

Low variability, snowmelt runoff inhibits coupling of climate, tectonics, and topography in the Greater Caucasus

Adam M. Forte[1], Joel S. Leonard[2], Matthew W. Rossi[3], Kelin X. Whipple[2], Arjun M. Heimsath[2], Lasha Sukhishvili[4], Tea Godoladze[4], Fakhraddin Kadirov[5]

[1]Department of Geology & Geophysics, Louisiana State University, Baton Rouge, LA, USA
[2]School of Earth and Space Exploration, Arizona State University, Tempe, AZ, USA
[3]Earth Lab, Cooperative Institute for Research in Environmental Sciences (CIRES), University of Colorado, Boulder, CO, USA
[4]Institute of Earth Sciences and National Seismic Monitoring Center, Ilia State University, Tbilisi, Georgia
[5]Institute of Geology and Geophysics of Azerbaijan National Academy of Sciences, Baku, Azerbaijan

Corresponding Author: Adam M. Forte (aforte8@lsu.edu)

Highlights

- New, comprehensive set of cosmogenic erosion rates from the Greater Caucasus
- Erosion rates show very nonlinear relationship with channel steepness
- Erosion-steepness relationship explained by stochastic threshold incision model
- Nonlinear relationship related to orographic controls on snowmelt runoff
- Precipitation phase may modulate degree of climate-tectonic coupling possible

Abstract

Hypothesized feedbacks between climate and tectonics are mediated by the relationship between topography and long-term erosion rates. While many studies show monotonic relationships between channel steepness and erosion rates, the degree of nonlinearity in this relationship is geographically variable. There is a critical need to mechanistically explain controls on this relationship in natural settings because highly nonlinear relationships imply low sensitivity between climate and tectonics. To this end, we present a carefully coordinated analysis of cosmogenic ^{10}Be concentrations in river sands paired with topographic, hydro-climatic, and tectonic data for the Greater Caucasus Mountains where topography is invariant along-strike despite large gradients in modern precipitation and convergence rates. We show that spatial patterns in erosion rates largely reflect regional tectonics with little influence from mean precipitation or runoff. The nonlinearity in the erosion rate – steepness relationship to arises from very

low runoff variability characteristic of snowmelt hydrology. Transitioning from rainfall- to snowmelt-driven runoff as mean elevation increases is common to many mid-latitude mountain ranges and the associated decrease in runoff variability may represent important, unrecognized dynamics inhibiting the sensitivity of tectonics to climate more broadly.

1. Motivation

The potential for dynamic coupling between climate and tectonics has driven decades of research. However, empirical data are equivocal with results both supporting and rejecting such coupling (e.g., Whipple, 2009). The extent to which climate can influence tectonics in fluvial landscapes depends both on the sensitivity of topography to climatic variables, like precipitation, and runoff and tectonic ones, like convergence and uplift rates (DiBiase and Whipple, 2011; Whipple, 2009; Whipple and Meade, 2004). If the relationship between topography and erosion rates is highly nonlinear, then large changes in erosion rates only drive slight changes in fluvial relief and the potential for two-way coupling is low (Whipple and Meade, 2004). In this study, we focus on daily runoff variability, which when paired with a threshold to incision, becomes a critical control on the form of the topography-erosion rate relationship (e.g., DiBiase and Whipple, 2011; Lague, 2014; Lague et al., 2005). Under this view, regions with extremely low runoff variability (e.g., due to snowmelt) should exhibit a highly nonlinear topography-erosion rate relationship. We examine this expectation in the Greater Caucasus (GC), where prior work demonstrates a lack of obvious climatic or tectonic influences on topography despite significant along-strike gradients in both (Forte et al., 2016). We present a large, new suite of basin-averaged ^{10}Be erosion rates along with detailed analyses of topography, tectonics, and hydroclimate to evaluate whether very low runoff variability in the GC explains the apparent disconnect between climate, tectonics, and topography. We then consider these results in the broader context of how the relative contributions from snowmelt versus rainfall runoff change as mountain ranges grow.

2. Background

2.1 Fluvial Incision Modeling and Climate-Tectonic Coupling

The rate of bedrock erosion by rivers, E [L/t] is often estimated using the stream power incision model (Lague, 2014) (SPIM):

$$E = KA^m S^n \tag{1}$$

where K [L^{1-2m}/t] is a constant encapsulating climate and substrate properties, A [L^2] is contributing drainage area as a proxy for discharge, S [L/L] is local river slope, and m and n are dimensionless constants related to erosional process, friction relationship, and width scaling (Lague, 2014). Within this framework, it is useful to consider a normalized metric of channel steepness which accounts for the expected co-variation of drainage area and slope. Normalized channel steepness index (k_{sn} [$L^{2m/n}$]) is an empirical relationship (Kirby and Whipple, 2012) of the form:

$$k_{sn} = A^{\theta_{ref}} S \tag{2}$$

where θ_{ref} is a dimensionless constant describing the concavity index of a channel. In the context of SPIM, θ_{ref} is equivalent to m/n at steady state. Substituting eq. 2 into eq. 1 generates a direct, if simple, prediction relating long term erosion rates, E, to the topography of a landscape as described by k_{sn} (Kirby and Whipple, 2012; Lague, 2014):

$$k_{sn} = K^{-1/n} E^{1/n} \tag{3}$$

At steady state, n governs the sensitivity of topography to changes in tectonics or climate whereby high values imply weaker coupling (e.g., Whipple and Meade, 2004). Globally, E-k_{sn} relationships vary widely and range from linear to highly nonlinear (Harel et al., 2016; Kirby and Whipple, 2012; Lague, 2014), necessitating consideration of this relationship at the landscape scale when evaluating potential climate-tectonic coupling.

While predictions from SPIM explain a variety of observations (e.g., Kirby and Whipple, 2012), its simplicity impedes interpretation of the shape of E-k_{sn} relationships. One promising alternative are models that incorporate event-scale runoff variability with erosion thresholds, i.e. a stochastic threshold incision model (STIM) (Campforts et al., 2020; Deal et al., 2018; DiBiase and Whipple, 2011; Lague et al., 2005; Scherler et al., 2017; Tucker, 2004) where the instantaneous incision rate I is expressed as:

$$I = K\bar{R}^m Q^{*\gamma} S^n - \Psi_c \tag{4}$$

$\bar{R}$ [L/t] is the mean runoff assuming mean discharge ($\bar{Q}$ [L^3/t]) divided by drainage area, $Q^*$is daily discharge divided by mean daily discharge, γ is the local discharge exponent, and Ψ_c is a threshold parameter that scales with the critical shear stress for incision (τ_c [$LM^{-1}T^{-2}$]) and substrate erodibility (k_e [$L^{2.5}T^2M^{-1.5}$]). Eq. 4 reduces to eq. 1 for a constant discharge ($Q^* = 1$) and zero threshold (Ψ_c=0). Under STIM, the long-term erosion rate, *E*, is the integration of eq. 4 over a distribution of discharges:

$$E = \int_{Q_c(k_s)}^{Q_m} I(Q, k_s) pdf(Q) dQ \tag{5}$$

where Q_c is the minimum discharge that exceeds τ_c, $Q_m$is the maximum discharge considered, and the $pdf(Q)$ is the probability distribution of discharge. A variety of probability distributions of daily discharge have been used, but here we follow Lague et al., (2005) in using the inverse gamma distribution:

$$pdf(Q^*) = \frac{k^{k+1}}{\Gamma(k+1)} exp\left(-\frac{k}{Q^*}\right) Q^{*-(2+k)} \tag{6}$$

where Γ is the gamma function and k is a variability parameter describing the shape of the distribution. Application of this version of STIM are well documented and thus we refer interested readers to prior studies (e.g., Campforts et al., 2020; Deal et al., 2018; DiBiase and Whipple, 2011; Lague, 2014; Lague et al., 2005; Scherler et al., 2017). In STIM, the degree of nonlinearity of the E-k_{sn} relationship fundamentally depends on the variability parameter, *k* (Lague, 2014; Lague et al., 2005) and predicts that settings with lower discharge variability and thus higher values of k will exhibit more nonlinear E-k_{sn} relationships.

2.2 Regional Background of the Greater Caucasus

The Greater Caucasus Mountains (GC) represent the northernmost extent of deformation caused by the Arabia-Eurasia collision. In the central portion of this collision, the GC are the main locus of shortening since plate reorganization at ~5 Ma (Allen et al., 2004). While the timing of reorganization coincides with rapid exhumation throughout the GC (e.g., Avdeev and Niemi, 2011; Vincent et al., 2020), large uncertainties remain as to the location, rates, and nature of major structures within the GC (e.g., Cowgill et al., 2016). Since ~1-2 Ma, active shortening largely stepped out from the main range and localized on a series of foreland fold-thrust belts along its northern and southern flanks. However, active shortening is kinematically linked to structures and continues to drive rock uplift in the main range (e.g., Forte et al., 2014, 2013; Mosar et al., 2010; Trexler et al., 2020). Modern convergence (Reilinger et al., 2006) and precipitation (Forte et al., 2016) rates vary by an order-of-magnitude along strike, with shortening increasing and precipitation decreasing eastward (Fig. 1). While along-strike patterns in convergence are complex (Fig. S1), we focus on the component accommodated along the southern range front because this is relevant to the samples we collected (Fig. 1). Whether modern geodetic velocities represent long-term geologic rates remains controversial (Forte et al., 2016), though geodetic rates of shortening are at least consistent with rates from the last 1-2 Ma (Forte et al., 2013; Trexler et al., 2020).

Theory suggests that along-strike variations in precipitation and convergence rates should lead to an eastward increase in elevations and local relief (Whipple and Meade, 2004), assuming direct translation of convergence to rock uplift. This is not observed in the GC and is not explained by potential confounding factors like glaciation and lithological heterogeneity (Forte et al., 2016). Instead, topography is relatively invariant along-strike with an across-strike pattern of lower relief flanks and a higher relief core (Forte et al., 2016) (Fig. 1). Prior studies attribute the across-strike gradient in topography to a northward increase in uplift rates along the southern flank of the GC with local maxima near drainage divides (Forte et al., 2015). Forte et al. (2016) also evaluated whether trends in mean precipitation were masking other important climate gradients (e.g., streamflow variability) that might better explain topographic patterns, to no avail. They concluded that invariant topography along-strike was either due to a (1) disconnect between modern tectonics and climate with the longer-term forcing, or (2) complex, co-varying relationships between the two. However, interpreting topography alone is fraught, and testing such hypotheses requires careful sampling of erosion rate data (e.g., DiBiase et al., 2010; Scherler et al., 2014), a key motivation for this study.

Prior estimates of exhumation and erosion rates in the GC largely come from low-temperature thermochronology (e.g., Avdeev and Niemi, 2011; Vincent et al., 2020, 2011) or modern sediment yields and provenance (e.g., Vezzoli et al., 2020). Thermochronology data, mostly concentrated west of 44°E, suggest older cooling ages along the lower relief flanks than the higher relief core, patterns that are broadly reflected in the topography (Forte et al., 2016). Exhumation rates are representative of the last ~5 Ma suggesting rates of ~1000 m Myr^{-1} in the core that decrease to <250 m Myr^{-1} towards the flanks (Avdeev and Niemi, 2011; Vincent et al., 2020). Over the modern era, erosion rates inferred from sediment yields and heavy mineral provenance imply similar average rates and spatial patterns, but with erosion rates near the range core >2000-3000 m Myr^{-1} locally (Vezzoli et al., 2020). At the millennial scale, there is only one published basin-averaged ^{10}Be erosion rate from the Inguri river in the western GC. The 1100 m Myr^{-1} rate (Vincent et al., 2011) is comparable to the long-term and short-term rates, though it averages across significant variations in steepness and major knickpoints, and thus hard to relate to topography in any meaningful way. Our new dataset seeks to fill this gap by reporting a large, new, millennial-scale, ^{10}Be erosion rate dataset that spans gradients in topographic relief in the GC.

3. Methods

To understand how well topography reflects erosion rates, we carefully sampled and measured cosmogenic ^{10}Be in quartz river sands (e.g., Bierman and Nichols, 2004) from 34 locally equilibrated, unglaciated basins (Fig. 1). Sampling was carefully paired with analyses of modern tectonics, topography, and hydrology of rivers to better assess predictions of SPIM and STIM fluvial erosion laws. Below, we summarize these methods. Where appropriate, we provide additional detail in the Supplement along with archival of raw data and algorithms in a GitHub repository.

3.1. Characterizing climate, tectonics, and topography

3.1.1 Modern Precipitation and Streamflow

Rainfall primarily comes from Tropical Rainfall Measurement Mission (TRMM) 3B42 data, and basin-averaged standard deviation of mean monthly snow cover is from MODIS MOD10C2. Data processing of both are described elsewhere (Forte et al., 2016). We supplement the rainfall data with a suite of ground based precipitation stations from the European Climate and Assessment Dataset (Klein Tank et al., 2002). Daily records of discharge, which we convert to runoff by dividing by drainage area (Fig. 2), for the Caucasus region comes from the Global Runoff Data Centre (GRDC) and was also originally presented elsewhere (Forte et al., 2016). We reprocess the runoff data here to remove basins whose variability may be artificially low due to dams and to describe variability as a power-law fit of the right tail of the distribution, which we describe in a later section.

Prior analysis of the GC runoff data found extremely low variability, which was speculatively linked to the dominance of snowmelt runoff (Forte et al., 2016). To better understand the cause of low daily runoff variability, we partitioned daily flows into annual, seasonal, and event components in each basin (Table S1). The annual component is inferred from the 365-day moving minima. The seasonal component is inferred from the 31-day moving minima minus the annual component. The event-driven component is inferred from the daily flows minus both the seasonal and annual components. Under this view, event flow effectively includes overland flow, shallow subsurface flow, and rain-on-snow. Depending on the basin, seasonal flows incorporate a mix of seasonal changes in groundwater storage, rainfall frequency, and/or snowmelt dynamics. The annual component reflects longer-term changes in groundwater storage. To develop a climatology of daily flows, we also calculate mean daily runoff as a function of day of year and apply a 31-day moving mean to smooth over the influence of historic events. Similar analyses on mean daily rainfall from TRMM are only used to determine the timing of peak rainfall in the main text, though full time series are shown in Fig. S23.

3.1.2 Modern convergence rates

To compare the erosion rates to modern convergence rates, we follow prior efforts which divided GPS velocities into either a Greater Caucasus or Lesser Caucasus domain (Avdeev and Niemi, 2011; Forte et al., 2014) and calculated average velocities along-strike using a sliding 50-km moving window (Fig. S1). Convergence between the Lesser and Greater Caucasus is the difference between these velocities along-strike. Our results are similar to prior estimates (Forte et al., 2014), but incorporate updated GPS velocities (Sokhadze et al., 2018). Additional details for the calculation of average velocities, convergence rates, and parsing of individual GPS stations into domains are provided in the Supplement (Figs. S1, S2).

3.1.3 Topographic metrics

Topographic analyses of individual basins were done using TopoToolbox (Schwanghart and Scherler, 2014) and TAK for TopoToolbox (Forte and Whipple, 2019). Specifically, we relied on 'ProcessRiverBasins' and various downstream tools within TAK to calculate basin-averaged statistics of topography and climatology. For basin-averaged topographic metrics, we use the SRTM 30-m DEM and calculated k_{sn} using a reference concavity of 0.5. While this reference concavity is appropriate for the GC (e.g., Forte et al., 2016), we tested whether the observed shape of the relationship between k_{sn} and ^{10}Be erosion rate was sensitive to the choice of reference concavity and found no demonstrable differences across a range of concavities from 0.3-0.6 (Fig. S9).

3.2. Cosmogenic Erosion Rates from Alluvial ^{10}Be Inventories

Prior to field sampling, we vetted basins that appear to be in local topographic steady-state (i.e., lacking major knickpoints; outside the influence of LGM glaciation) so that basin-averaged ^{10}Be erosion rates could be reliably related to k_{sn} (Fig. S3). This analysis motivated the sampling of 76 basins across the southern range front of the

Greater Caucasus. From these, a subset of 47 were processed for erosion rates (Table S2). Low abundance of quartz and difficulty in processing some samples due to lithology (see discussion in Supplement) resulted in usable amounts of quartz for 34 samples. For each sample, we selected the 0.25-1 mm size fraction and used a combination of traditional HF and HNO_3 leaches and the ‘hot phosphoric acid’ technique (Mifsud et al., 2013) to isolate and purify quartz. Additional details for quartz purification are described in the Supplement. Samples were spiked with either commercial or custom low-background ^{9}Be carrier, Be was extracted through liquid chromatography, and BeO was analyzed by accelerator mass spectrometry at PRIME Lab, Purdue University. To convert ^{10}Be concentrations into erosion rates, we calculated effective latitude and elevations to determine basin-averaged ^{10}Be production rates (Portenga and Bierman, 2011), and used these in v3.0 of the online calculator formerly known as the CRONUS calculator (Balco et al., 2008). Erosion rates are reported for a time independent scaling scheme (Stone, 2000). Additional details with regards to site selection, sample processing, and erosion rate calculations are provided in the Supplement. All relevant parameters needed to reproduce erosion rates are provided in Table S3.

Due to low quartz yields, we also carefully examined the bedrock geology for each basin (Fig. S24-S57, Table S4) to assess the influence of variable quartz sourcing on derived erosion rates. By recalculating topographic metrics and erosion rates after removing portions of basins with lithologies unlikely to provide quartz, we found no meaningful difference in the E-k_{sn} patterns (Fig. S4, Table S3). We also considered the end-member scenarios where we assume that quartz is entirely sourced from the upper or lower 50% of each basin and recalculated topographic metrics and erosion rates (Fig. S4, Tables S3). Again, we found little difference in E-k_{sn} patterns that would change the central conclusions of this work.

3.3 Numerical Modeling of River Incision

3.3.1 Parameterization of SPIM

To assess which SPIM parameters best characterize the relationship between channel steepness and ^{10}Be erosion rates, we fit eq. 3 to the measured E and k_{sn} data.

To do this, we linearize eq. 3 using a log-transform and then fit the data using the orthogonal distance regression (ODR) algorithm in SciPy. To estimate ranges of acceptable fits, we tested both a bootstrap and Monte Carlo method. The latter is similar to the method used by Adams et al. (2020). While results are comparable, the bootstrap approach results in wider estimates of uncertainty. As such, we report uncertainties using the bootstrap fits as more conservative estimates. Additional details of fitting are laid out in the Supplement. In fitting the data, we exclude data from one basin whose uncertainty exceeds its mean value (Fig. S11). We also test the sensitivity of fits to the two highest erosion rates. While removal of these two rates suggest a lower n, the range of uncertainties inclusive and exclusive of these data substantially overlap (Fig. S11). Given the lack of any meaningful reason to exclude these high erosion rate data, all reported fits include these high erosion rate basins.

3.3.2 Parameterization of STIM

STIM is a more complex model than SPIM and thus requires calibration of a larger number of parameters. Prior studies provide more detailed discussion of the derivation of STIM and reasonable parameter values (Campforts et al., 2020; Deal et al., 2018; DiBiase and Whipple, 2011; Lague et al., 2005; Scherler et al., 2017). For this work, parameter values are summarized in the Supplement and many (k_t, ω_a, ω_s, α, β, a) are set to previously used values (e.g., DiBiase and Whipple, 2011). The five parameters we vary or calibrate in our analysis are; $\bar{R}$, k, k_w, τ_c, and k_e, each of which are justified below.

Because none of the ^{10}Be basins are gauged, we generalize stochastic parameters in gauged GRDC basins for attribution to ungauged ^{10}Be basins (Figs. 3-4). To estimate $\bar{R}$ in ungauged basins, we use the relationship between $\bar{R}$ (Fig. 3) and TRMM mean daily rainfall (*MDP)* in gauged basins. To do this, we first converted mean daily discharge to mean daily runoff assuming a linear relationship between drainage area and discharge (Fig. 2). Next, we used ground based precipitation stations (Klein Tank et al., 2002) to bias-correct the TRMM 3B42 data and derive *MDP* for each gauged basin (Fig. 3). The linear fit between *MDP* and runoff ratio ($\bar{R}/MDP$) for gauged basins is used to estimate $\bar{R}$ in ungauged basins (Fig. 3). We use a linear fit to runoff ratio as opposed between MDP and $\bar{R}$, because the former is better approximated with a linear fit than the latter.

Runoff variability is characterized using the shape parameter (k) of the daily distribution, which is estimated by fitting a power-law to the upper 1% of flows in each gauged basin (Fig. 2). These results are generalized to ungauged basins using linear regressions to the maximum elevation of the basin and the standard deviation of monthly mean snow cover (Fig. 4, Table S3). We found these two metrics be the best proxies for *k* after testing a variety of topographic and climatic metrics. Given that the two metrics make slightly different predictions for individual basins and lack a clear basis to choose one, we averaged the two estimates to derive k values for the ungauged basins.

The scaling between channel width and discharge (k_w) is an important, and hard to constrain, hydraulic geometry relationship that strongly controls the shape of the *E*-k_{sn} relationship predicted by STIM (Lague, 2014). Channel width (w) is typically related to discharge (Q) using the function:

$$w = k_w Q^{\omega_a} \tag{7}$$

where ω_a is a constant we set to 0.5. Following DiBiase and Whipple (2011), we set the value of k_w to 15 but test its importance by comparing observed channel widths to predicted widths for both the mean and 2-year flows (Fig. 5, Fig. S12-S13). We measure channel widths for 26 of the 34 sampled basins using satellite imagery and ChanGeom (Fisher et al., 2013). We were unable to measure channel widths for all basins because of poor imagery and/or density of tree cover. This analysis suggests that k_w of 15 largely encompasses observations and therefore we set this parameter as a constant for all basins (Fig. 5). Additional details on channel width analyses can be found in the Supplement.

Finally, k_e and τ_c control the magnitude of the threshold parameter (Ψ_c) in STIM. Given the lack of direct constraints on either and the infeasibility of leaving both as free parameters, one needs to be fixed to calibrate the model. Although we primarily report solutions where k_e is free and τ_c is fixed, we do test the alternative case (Fig. 5). While

values of k_e or τ_c differ between optimizations, the *E*-k_{sn} pattern is unchanged. Our goal is find a single, best-fit value of k_e that can be used as representative of the entire erosion rate dataset. To arrive at this, we first treat each basin independently and estimate k_e. Following DiBiase and Whipple (2011) and fixing τ_c at 45 Pa, we used STIM to find k_e for each basin that most closely reproduces measured *E* for the known value of k_{sn} and estimated k and $\bar{R}$ (e.g., Fig. 3-4). To account for uncertainty in both k_{sn} and *E*, we generate a synthetic distribution of 500 k_{sn} and *E* values drawn using the mean and uncertainties of individual basin k_{sn} and *E* values. The best-fit k_e is the one that minimizes the misfit between synthetic pairs of k_{sn} and *E* values. The median of the population of optimized k_e values is used to estimate an acceptable, single k_e value to apply to the landscape (Fig. 5). This approach assumes limited influence of lithology on k_e, which is consistent with prior results from the GC (Forte et al., 2016, 2014) and reinforced by the lack of correlation between the optimized k_e values and lithology (Fig. S15). We emphasize that while some studies applying STIM to cosmogenic erosion rates attempt to constrain τ_c from grain size measurements (DiBiase and Whipple, 2011), the challenge of obtaining these kinds of data prompts many studies like ours to simply assume a reasonable grain size and corresponding τ_c (Campforts et al., 2020; Scherler et al., 2017). Additional details of k_e and τ_c optimizations are provided in the Supplement and associated algorithms are archived in the GitHub repository.
Alternatively, we also independently estimate values for $\bar{R}$, k, and k_e by treating these as free parameters and fit STIM to the measured k_{sn} and *E* values using an ODR fit. The associated algorithm for performing this fit is archived in the GitHub repository.

4. Results

4.1 Relating Erosion Rates to Topography

Erosion rates, *E*, vary from 33-5610 m Myr^{-1} (Figs. 7). Rates do not have a simple relationship with along-strike position (Fig. S6), but appear to increase monotonically with LC-GC convergence rates (Forte et al., 2014; Kadirov et al., 2012; Reilinger et al., 2006; Sokhadze et al., 2018) (Fig. 1C, 6C, S5). Across-strike, *E* systematically increases from the southern flanks of the range towards the core, reaching a peak south of the topographic crest (Fig. 7B). Despite the wide range of *E*, all data lie on a single, highly nonlinear relationship between k_{sn} and E (Fig. 8A). Similar relationships exist between E and mean basin slope due to the quasi-linear relationship between k_{sn} and slope in this setting (Fig. 8C, S9). Remarkably, over erosion rates from ~300 to >5000 m Myr^{-1}, channel steepness is essentially invariant, ranging between ~300-500 m (Fig. 8). While there is substantial scatter in these high E and k_{sn} basins, this is not unusual for these kinds of datasets. Moreover, detailed interrogation of potential confounding factors reveals no meaningful way to subdivide these data into different physically interpretable populations (Fig. S8).

4.2 River Incision Modeling

Fitting data with SPIM (eq. 3) suggests an n of 3.1 to 4 with a median value of 3.5 (Fig. 8, Fig. S11). This is in the range of n found elsewhere, but well above the global mean value of ~2.5 (Harel et al., 2016; Lague, 2014). To see if direct relationships exist between mean climate and either E and k_{sn}, Figure 8B shows the relationship between mean rainfall and erosion rate color-coded by channel steepness. While E does not systematically vary with MDP (Fig. 8B) or $\bar{R}$, both E and k_{sn} do increase where variability decreases (i.e., increasing k) (Fig. 8A). Given this outcome, we turn to STIM which explicitly accounts for daily runoff variability, to see how well it explains the strong nonlinearity in the empirical E-k_{sn} relationship.

We use measured E and k_{sn} and estimated $\bar{R}$ and k to estimate k_e for each sampled basin. Figure 6 shows these results and suggests that optimized k_e varies over six orders of magnitude and quasi-linearly varies with $\bar{R}$ (Fig. 6). We do not think this reflects the true variation in k_e because values show no clear relation with lithology (Fig. S14). Rather, by accounting for inter-basin variation in $\bar{R}$ and k and holding other variables constant, $k_e$is the only free parameter that can adjust in the regression analysis to account for variations among basins. Other model parameters related to the incision threshold (τ_c) and channel width scaling (k_w, ω_a, and ω_s) undoubtedly vary from basin to basin, likely explaining why optimizing only k_e leads to such a large range of values. We suspect channel width scaling to be a key source of inter-basin heterogeneity. However, because we do not observe any clear relationship between channel width and either $\bar{R}$ or *E* (Fig. S13), we do not think this important source of uncertainty is systematically biasing STIM predictions.

To further explore variations in the parameterization of k_e, we compare results to an alternative optimization where τ_c is the free parameter and k_e is fixed (Fig. 7C-D). This exercise also produces an apparent relationship between the free parameter (τ_c in this case) and $\bar{R}$, albeit over a relatively narrower range of values. Whether optimizing for k_e or τ_c, the basic result is that STIM predictions for each basin retain a runoff dependence that cannot be resolved with our data. Interestingly, this cross-correlation does not appear for runoff variability, where no relationship emerges between k and optimized k_e or τ_c (Fig. 6A or C). Furthermore, neither optimized $k_e$or τ_c systematically vary with erosion rate or topography of the basins (Fig. S15). The wide range of optimized k_e or τ_c and their correlation with $\bar{R}$ may reflect dynamics not included in STIM like rules for sediment flux and bed cover (Sklar and Dietrich, 2006) or other climatic influences on bed erodibility (Murphy et al., 2016), important caveats that motivate future work .

For this study, we use the range of optimized k_e values to estimate a single k_e value that is suited to landscape-scale analysis. Applying STIM using median values of estimated $\bar{R}$, k, and k_e generates an *E*-k_{sn} relationship remarkably similar to measured values (Fig. 8). The alternative approach of using an ODR fit to the measured k_{sn} and *E* to estimate $\bar{R}$, k, and k_e had very little impact on model results, independently suggesting similar values for these three parameters as those found from the median value approach (Fig. 8). In comparison to SPIM, both applications of STIM performs similarly in goodness of fit metrics (Fig. 8, S16). In detail, the different models deviate from measured values in different ways (e.g., SPIM shows better correspondence to lower *E* and k_{sn} data than STIM and vice versa; Fig. 8A). Despite comparable goodness of fit, we favor STIM results because it enables a data-driven interpretation to the highly nonlinear relationships observed.

5. Discussion

5.1 Tectonic Implications for the Greater Caucasus

Our new cosmogenic erosion rates in the GC are broadly consistent with prior million-year and decadal rates. All suggest systematic increases in *E* toward the core of the range with maximum *E* exceeding 1000-2000 m Myr^{-1} (Avdeev and Niemi, 2011; Vezzoli et al., 2020; Vincent et al., 2020, 2011), though our highest rates are somewhat faster than prior estimates. The broad agreement between *E* and GC-LC convergence rates suggest that millennial scale *E* faithfully records modern tectonic forcing (Fig. 6, S5). While the degree to which modern GPS velocities (Kadirov et al., 2012; Reilinger et al., 2006; Sokhadze et al., 2018) reflect geologic rates remains controversial (Forte et al., 2016), they are representative of geologic rates of shortening over the last 1-2 Ma (Forte et al., 2013; Trexler et al., 2020). Using this as a baseline, spatial patterns in cosmogenic *E* are consistent with the expected vertical components of GC-LC shortening rates applied to north-dipping structures with reasonable dips (Fig. 6), though it is emphasized that the geometry of structures in the interior of the GC are not well constrained (e.g., Cowgill et al., 2016; Forte et al., 2014). While substantial scatter exists, likely due to local structural complexity, this result strongly contrasts with the poor correlation between *E* and mean rainfall or estimated runoff (Fig. 8). As such, a simple climatic control on *E* in this setting is unsupported and thus requires more careful consideration of hydro-climatic controls on bedrock river incision itself, the focus of the rest our discussion.

5.2 Strengths and Limitations of STIM

The ability of STIM to reproduce observed E-k_{sn} relationships (Fig. 8, S16) suggests that the shape of this relationship in the GC is aided by considering the local hydro-climatology, namely the systematic decrease in runoff variability with elevation (e.g., Fig. 4B). We relate these orographic patterns in variability, and thus the extreme nonlinearity of the E-k_{sn} relationship, to the importance of snowmelt. This is consistent with previous interpretations of the GC (Forte et al., 2016) and the more general observation that mountain regions with a large snow fraction tend to have lower event-scale runoff variability (e.g., Rossi et al., 2016) as the dominant flood generating mechanism changes from rainfall to snowmelt runoff (e.g., Berghuijs et al., 2016). As such, we first ask whether STIM is well suited to this modeling task.

The conceptual framing for STIM (Lague et al., 2005; Tucker, 2004) was built around rainfall events that trigger runoff over the span of hours to days, not months. Stochastic models of streamflow can be similarly built for snowmelt processes as long as they account for the transient accumulation and release of snow water (Schaefli et al., 2013). And while there have been some efforts to integrate these differing drivers of runoff variability into a STIM framework (e.g., Deal et al., 2018), the complex dynamics of long duration, snowmelt hydrographs on sediment entrainment, deposition, and bedrock erosion (e.g., Johnson et al., 2010) is not well represented by the probability distribution of flows alone. Nevertheless, with an eye towards incremental addition of complexity to SPIM-inspired models of bedrock river incision, we view accounting of the probability distribution of flows as a necessary step, with the caveat that interpretations of incision thresholds may be more fraught when the timescales of events are long.

5.3 Hydro-climatology and STIM Parameterization

STIM unpacks the bulk treatment of climate in SPIM by characterizing climate using two parameters ($\bar{R}$ and k), a simple treatment of hydrology ($Q = R * A$), and an assumed probability distribution of daily mean runoff (inverse gamma distribution). In contrast to prior efforts showing a rough inverse relationship between mean runoff and runoff variability (e.g., Molnar et al., 2006; Rossi et al., 2016), the outsized role of snowmelt in the GC makes such simplifications in the GC unwarranted (Figure 9A). To characterize hydro-climatic regimes, we used k-means cluster analysis on estimated $\bar{R}$ and k values for sampled basins (Fig. 9B). Additional details are provided in the Supplement, but this analysis suggests our data is best explained by three clusters (e.g., Fig. 9A, S17). Cluster 1 has moderate $\bar{R}$ (< 4 mm/day) with very low variability (k>4). Cluster 2 has moderate $\bar{R}$ with low variability (2>k<4). Cluster 3 has high $\bar{R}$ (>4 mm/day). Clusters were used both to evaluate model fits (Fig. 9) and to aid interpretation of the underlying driver for differences in the runoff between basins (Fig. 10), which are discussed in turn below.

First, we consider model performance when clusters are considered separately. Using the median values of $\bar{R}$ and k for each cluster but keeping k_e fixed to the population median, we model each cluster using STIM (Fig. 9D). This approach explains channel steepness patterns in low runoff basins (Clusters 1 and 2), but not in high runoff basins (Cluster 3, Fig. 9D). Spatial patterns in *E* for Cluster 3 are consistent with the tectonic forcing (e.g., Fig. S20) suggesting that k_{sn} is anomalously high for at least three of the fours basins in this cluster (i.e., those in Fig. 9D that lie substantially above the modeled STIM relationship). Lithological differences do not explain anomalously steep basins (e.g., Fig. S8) indicating that other model parameters must differ for these basins and/or vary systematically vary with runoff, a finding supported by where this cluster falls in the relationship between $\bar{R}$ and k_e (Fig. 9C). Nevertheless, Clusters 1 and 2 represent the bulk of the data and show that subsampling the population by differences in runoff variability is comparable to or improves upon STIM predictions derived from the population as whole (Fig. 10, S21).

Next, we relate the clusters to hydro-climatological controls. Figure 10A shows the smoothed mean daily runoffs as a function of time of year. In general, we interpret the strong seasonal signals in the GC as indicative of a dominant component of snowmelt runoff, especially when maxima occur in the summer, though caution is warranted where rainfall also peaks in the summer. Cluster 1 basins show a strong seasonal signal that is systematically offset from peak precipitation. All these basins have very low baseflow in the fall and winter. Cluster 2 basins exhibit muted to non-existent seasonality. These basins show less systematic relations to the timing of peak precipitation, though the overall phase lag is lower than in the other two clusters (Fig. 10A, S23). Cluster 3 basins all show strong seasonality and a systematic offset with the timing of precipitation, like observed in Cluster 1. However, baseflow in the fall and winter is typically very high compared to Cluster 1 and some lower elevation basins show a second, lower peak in runoff in the winter. Regardless of cluster, higher elevation basins typically show summer seasonality, reinforcing our interpretation that snowmelt is the dominant driver of seasonal flows throughout the Caucasus region.

Figure 10A does not fully characterize the regularity of flows because data were smoothed to develop a seasonal climatology. To probe whether and how well streamflow seasonality explains the runoff variability parameter, *k*, we partitioned time series data into three components: event, seasonal, and annual fractions which together sum to the total water fluxing through each river. For gauged basins, the seasonal component was the strongest and only correlate to daily runoff variability, especially for basins in the GC proper (Fig. 10B). Given that we attribute the seasonal component to spring/summer snowmelt with modest contributions from seasonal rainfall in some basins, we interpret patterns in runoff variability to be principally driven by the contribution of snowmelt to runoff. Thus we interpret that our application of STIM is accounting for orographic patterns in runoff variability that embed the long hydrologic response times associated with snowmelt runoff (Deal et al., 2018).

5.4 Implications for Interactions Among Climate, Tectonics, and Topography

The nonlinearity of the E-k_{sn} relationship in the GC explains why prior work (Forte et al., 2016) failed to recognize the influence of either precipitation or convergence gradients in the topography of the range (e.g., Fig. 1). Millennial scale erosion patterns are concordant with convergence rates and proximity to the core of the range (Fig. 7, S5). The similar width of the range along-strike (Forte et al., 2014) (Fig. 1) and the low sensitivity of channel steepness to E exceeding 300-500 m Myr^{-1} (Fig. 6A) explains why topography (e.g., mean elevation and local relief) is relatively invariant along-strike. STIM helps reconcile apparently large contrasts in mean annual precipitation and runoff between basins (Fig. 8B) by only considering the role of flows above the incision threshold. While we recognize that simplistic representation of events in STIM does not fully capture seasonal dynamics in the GC (e.g., Fig. 10, S23), the general result that low variability runoff leads to highly nonlinear E-k_{sn} relationships (DiBiase and Whipple, 2011; Lague, 2014; Lague et al., 2005) provides a satisfying explanation for the lack of a clear climate signal in the topography.

Our hypothesized link between the extreme nonlinearity in the E-k_{sn} relation and low variability snowmelt runoff has interesting implications. Under modern climate, only tributary basins on the low elevation and low erosion rate flanks of the range should be topographically sensitive to either climatic or tectonic changes. These areas: (1) have higher runoff variability due to a lesser influence of snowmelt (Fig. 8-10), and (2) are in the quasi-linear portion of the E-k_{sn} relationship (Fig. 8). Conventional approaches toward accounting for orographic precipitation in landscape evolution have focused on elevation-dependent fluxes of mean annual rainfall (Bookhagen and Burbank, 2006) or snowfall (Anders et al., 2008). This work highlights the critical role of the transition from rainfall- to snowmelt- driven hydrology in mediating runoff variability itself (Rossi et al., 2020), an important complexity rarely considered in landscape evolution studies. Transitioning from rainfall- to snowmelt- driven hydrology is dictated by the elevation distribution within a mountain range and presents a possible direct relation between climate and erosion rates in orogenic systems, albeit not in the traditional sense where there is a positive correlation between erosion and precipitation or runoff rates (Ferrier et al., 2013) . Importantly, a snowmelt control on runoff variability may be relevant to many mountain ranges where the growth of topographic relief has undermined the erosive ability of higher mean annual precipitation via distributing flows over longer duration snowmelt events.

6. Conclusions

We present a large suite of new basin-averaged ^{10}Be erosion rates from the Greater Caucasus that are consistent with longer term exhumation and shorter-term decadal scale rates. Erosion systematically varies with convergence rates between the Greater Caucasus and Lesser Caucasus and is uncorrelated to mean annual rainfall, favoring a tectonic control on erosion rates. The relationship between erosion and channel steepness is extremely nonlinear in this setting. However, careful consideration of regional hydro-climatology incorporated into a stochastic threshold incision model of river incision reveals that extremely low variability, snowmelt runoff is driving this nonlinearity thus explaining why prior efforts failed to recognize a clear climatic imprint on topography in the mountain range.

Our results also highlight the importance of both: (1) considering regionally constrained relationships between topography and erosion when assessing potential climate-tectonic interactions, and (2) understanding the underlying mechanism(s) setting that form. In the Greater Caucasus, significant climate-tectonic interactions are precluded because topography becomes insensitive to changes in forcing at uplift rates exceeding 300-500 m Myr^{-1}. This is in contrast to other settings where relationships between erosion and topography may be more linear. We emphasize that the observed nonlinearity between erosion rates and channel steepness in the GC is not a global solution to an apparent lack of coupling between climate and tectonics. Rather, the wide range of such relationships around the world likely reflects important landscape specific, hydro-climatic details that must be considered when applying erosion models. Our results also show that spatial and temporal patterns in precipitation phase that alter flood frequency may be an underappreciated governor on the degree of climate-tectonic coupling possible in mid-latitude mountain ranges not heavily influenced by glacial erosion.

Acknowledgements

This work was supported by the National Science Foundation grant EAR-1450970 to A.M.F. and K.X.W. We thank Charles Trexler and Alexander Tye for collecting a small subset of the samples used in this analysis; Eric Cowgill and Nathan Niemi for help and advice related to this project both in and out of the field; Dachi Injia, Giga Ugrekhelidze, Davit Kapanadze, and Zurab Javakhishvili for assistance in the field; and Byron Adams and Roman DiBiase for helpful discussions and sharing codes. We acknowledge the GRDC for providing runoff data, available here (https://www.bafg.de/GRDC/EN/Home/homepage_node.html). We also acknowledge the existence of two anonymous reviewers of an earlier draft of this manuscript.

Data Availability

The authors certify that all data necessary to reproduce the key findings of this paper are presented in the manuscript or its supplement. We additionally provide the majority of the data tables as plain text, shapefiles of the ^{10}Be basins, the GRDC basins, some select rasters that are generally not easily available, and many of the analysis scripts in a GitHub repository (https://github.com/amforte/Caucasus_Erosion DOI: 10.5281/zenodo.4629789)

Figures

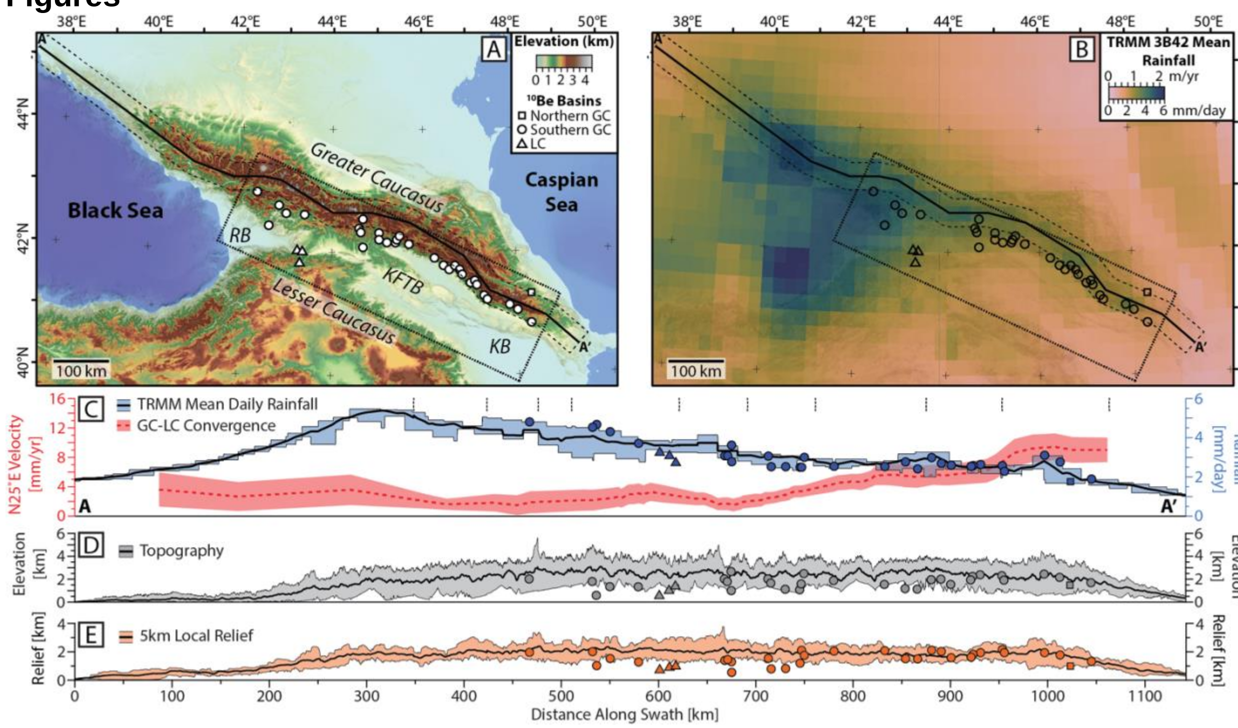

Fig 1. (A) Regional map with location of alluvial cosmogenic ^{10}Be samples (white symbols) within the Greater and Lesser Caucasus (LC). Line A-A' and corresponding box outline 50-km wide swath referenced in other figures and is centered on the topographic crest of the range. Dotted rectangle is outline of Fig 2A. KFTB – Kura Fold Thrust Belt, KB – Kura Basin, RB – Rioni Basin. (B) TRMM 3B42 mean daily rainfall (Forte et al., 2016). (C) Blue shaded region is maximum and minimum rainfall within the swath in panel B (line is mean value). Blue symbols are mean rainfall in sampled basins. Red shaded region is estimated convergence rates between the Greater and Lesser Caucasus along the southern margin of the Greater Caucasus, and id largely similar to that calculated by Forte et al., (2014). It was recalculated to include more recent GPS data (see Supplement and Figs. S1 and S4 for details). (D) Swath of topography. Symbols are mean elevation within sampled basins. (E) Swath of local relief using a 5-km radius circular moving window. Symbols are mean relief within sampled basins.

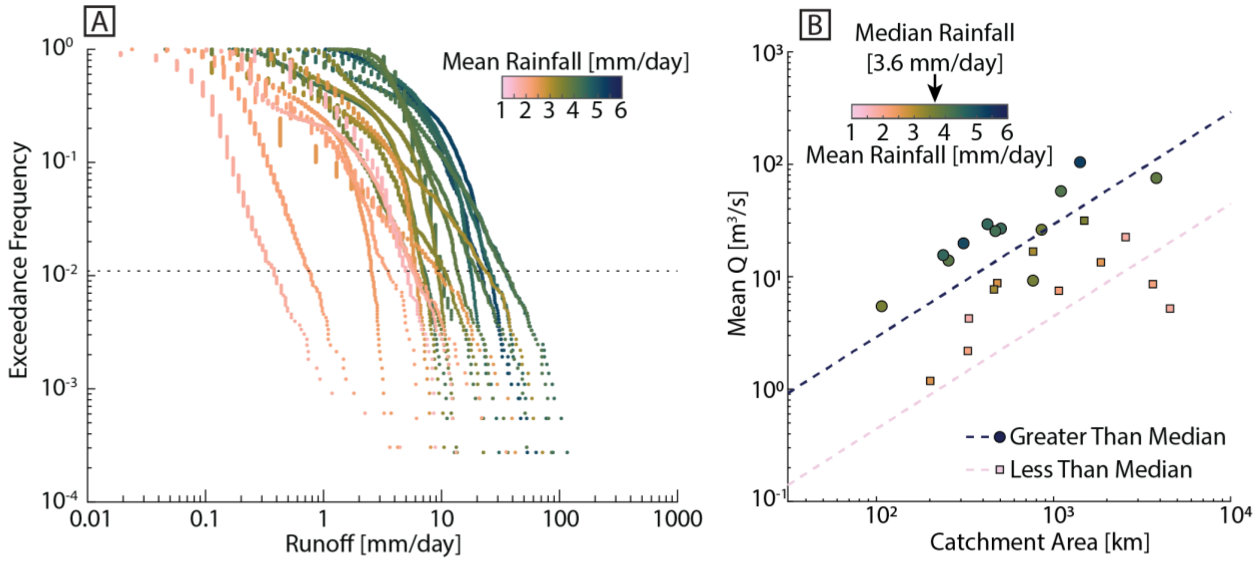

Fig 2. (A) Exceedance frequency versus daily runoff for each GRDC basin and colored by mean rainfall estimated from TRMM 3B42. Runoff calculations assume a linear scaling with drainage area, see 2C. (B) Mean discharge versus drainage area colored by mean rainfall for each GRDC basin. Also shown are linear fits of all basins with mean rainfall greater or less than the median value of all GRDC basins. The quasi-linear relationship between discharge and drainage area, after parsing by mean rainfall, is consistent with a linear scaling of runoff ($\bar{Q} = \bar{R}A$).

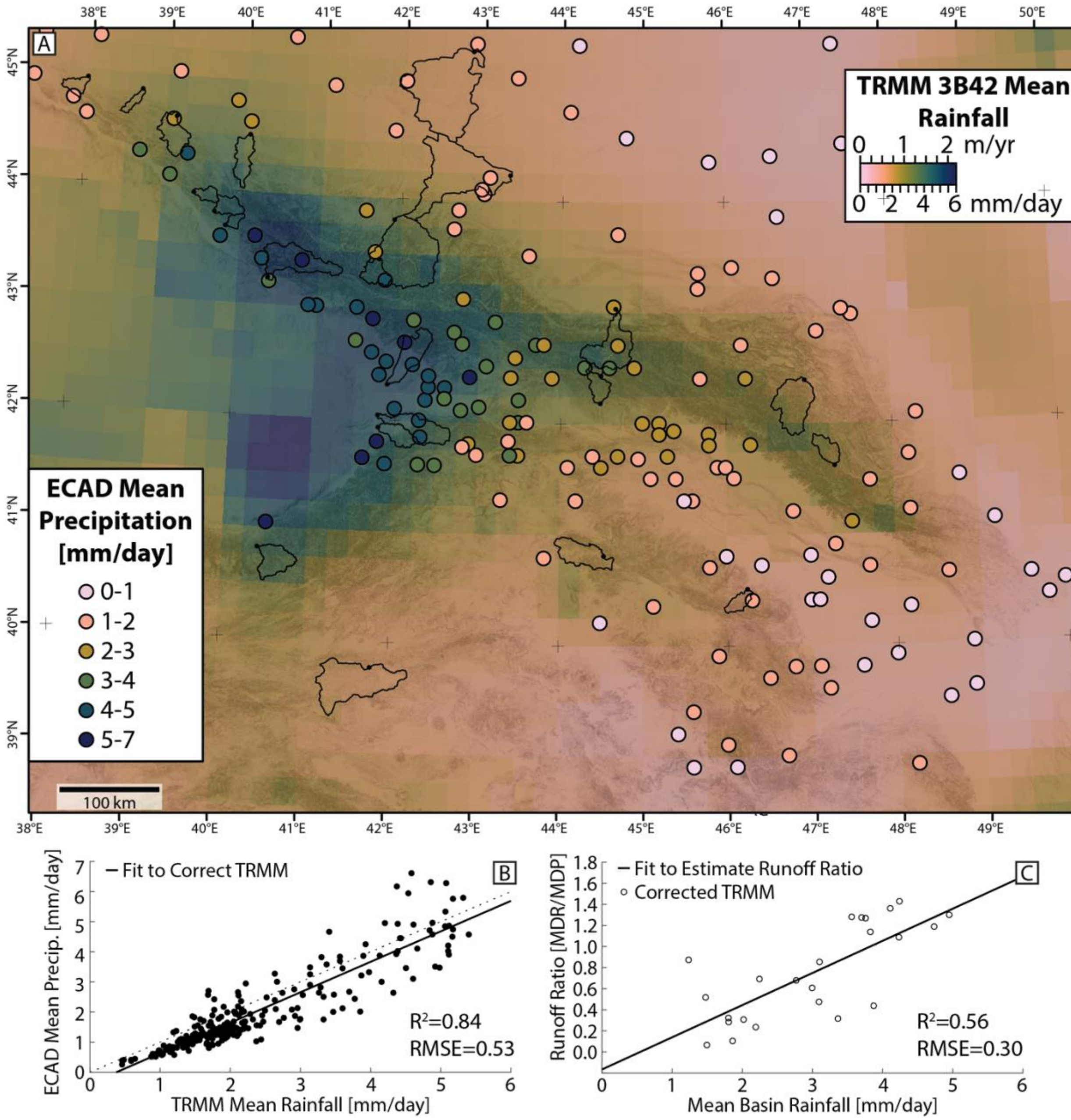

Fig 3. (A) Map of TRMM 3B42 mean rainfall averaged over the period of 1998-2012 (Forte et al., 2016). Overlain are individual precipitation stations from ECAD (Klein Tank et al., 2002) colored by mean daily precipitation. The time interval of averages varies by station. Basin outlines are GRDC basins used in the analysis. (B) Plot of TRMM mean pixel values vs ECAD mean station values (dashed line is 1:1; solid line is linear fit used to correct TRMM to station observations). (C) Relationship between mean basin precipitation (from corrected TRMM and runoff ratio for GRDC basins. Solid line is the linear fit to this data used to estimate runoff ratio in unknown basins. Note that this implies runoff ratios for some basins that exceed 1, as previously noted by Forte et al. (2016). This is discussed in the Supplement and an alternative solution where runoff

ratios are capped at 1 is explored. This alternative solution does not change the result, so we do use the solution shown here.

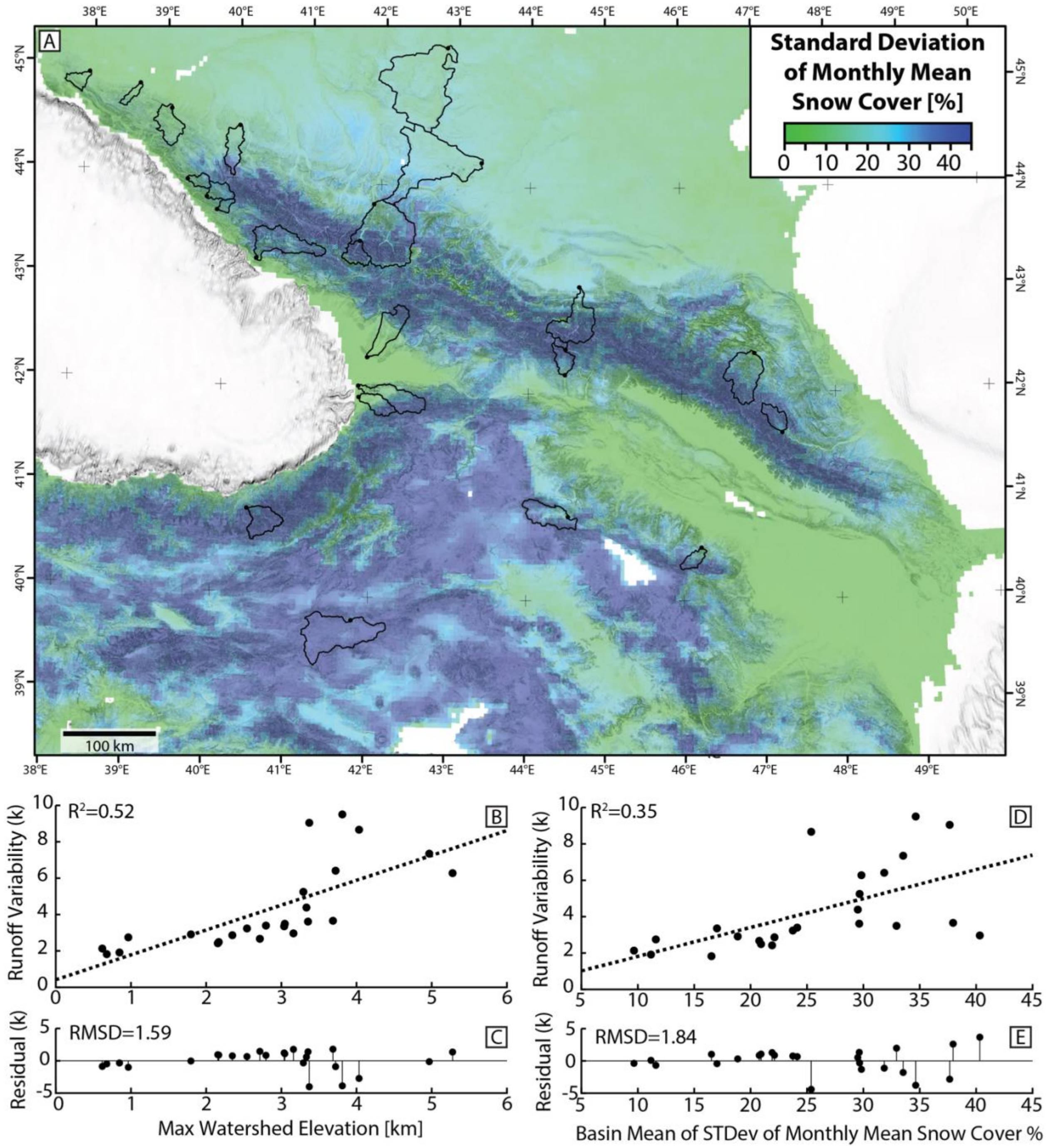

Fig 4. (A) Map of standard deviation of monthly mean snow cover as calculated from MODIS data (Forte et al., 2016). Basin outlines are GRDC basins used in the analysis. (B) Linear relationship between variability within GRDC basins and the maximum elevation of the gauged basin. (C) Residual on linear fit in 4B. (D) Linear relationship between variability within GRDC basins and the mean basin value of standard deviation

of monthly mean snow cover. (E) Residual on linear fit in 4D. Note that we use the average of these two relationships to determine variability for ungauged basins.

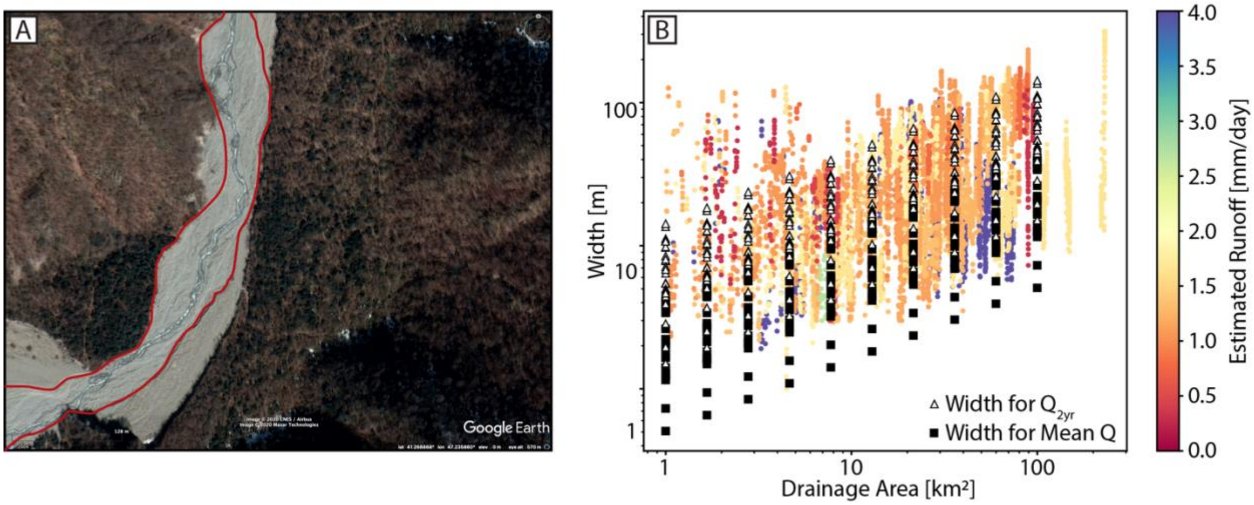

Fig 5. (A) Example of channel width as measured on satellite imagery from Google Earth. (B) Measured widths (dots colored by estimated runoff of each basin) and predicted widths using k_w = 15 and either the mean discharge or the 2-year flood (black symbols) as a function of drainage area. An un-interpreted version of 5A is provided in Fig. S12 and additional comparisons between width and drainage area scaling are provided in Fig. S13.

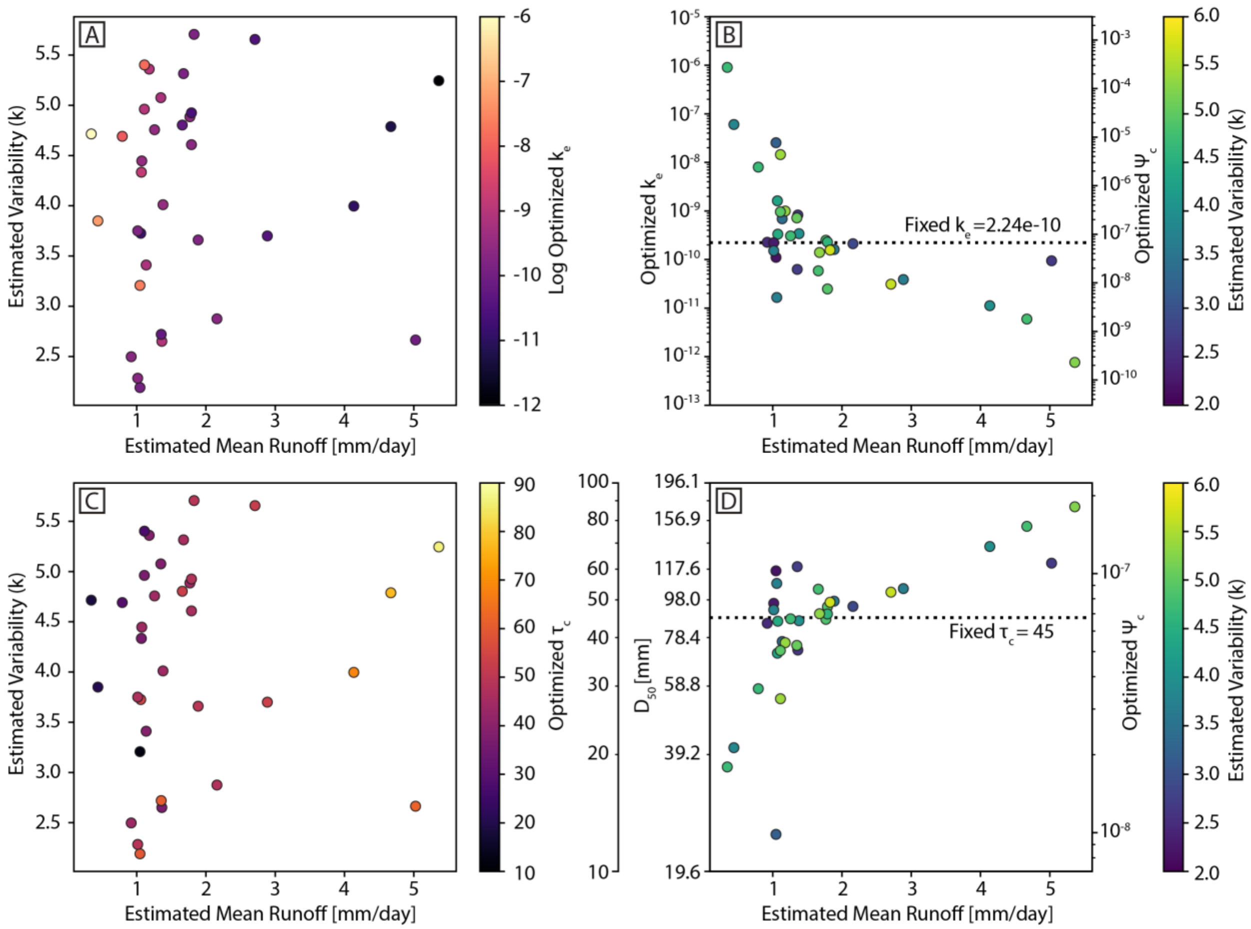

Fig 6. Results of optimizing either k_e with a fixed τ_c of 45 Pa (A & B) or τ_c with a fixed k_e of 2.24e-10 (B & C), see text for additional discussion. (A) Relationship between estimated variability (k) and estimated mean runoff ($\bar{R}$) colored by the optimized k_e. (B) Relationship between optimized k_e and estimated $\bar{R}$. The conversion between k_e and the threshold parameter Ψ_c (using the fixed τ_c of 45 Pa) is shown with the right-hand y-axis. (C) Same as 6A but colored by optimized τ_c. (D) Relationship between optimized k_e and estimated τ_c. Equation S19 is used to convert between τ_c and D_{50} and assumes a shields parameter of 0.3. As in 6B, conversion between τ_c and the threshold parameter Ψ_c (using the fixed k_e of 2.24e-10) is shown with the right-hand y-axis.

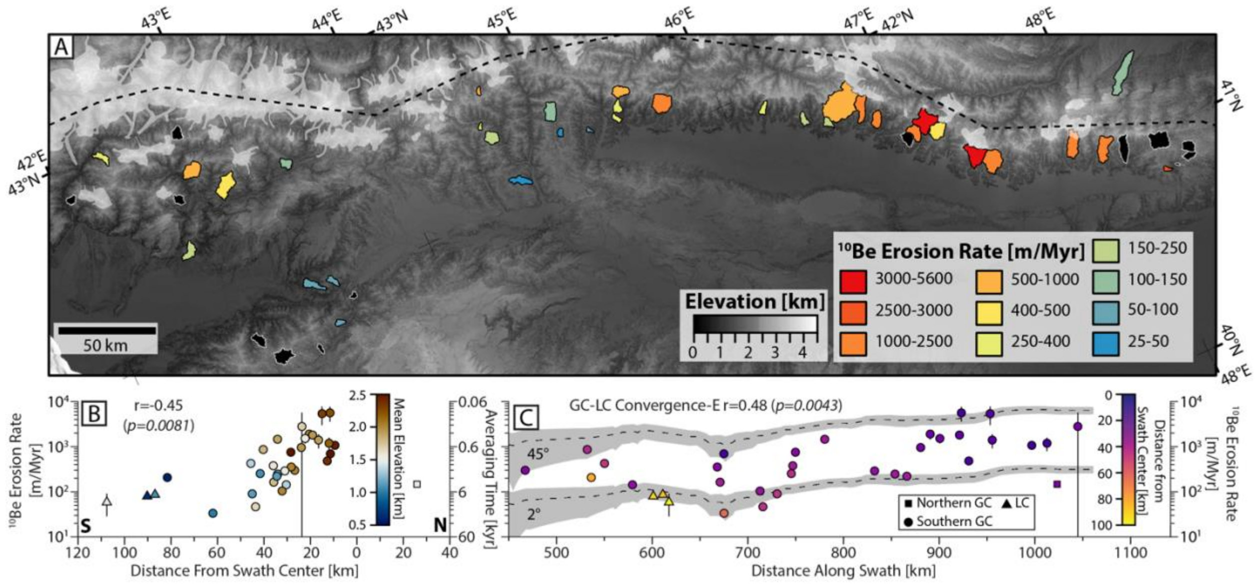

Fig 7. (A) Cosmogenic ^{10}Be erosion rates for sampled basins. Black basins indicate unsuccessful samples (insufficient quartz yield; see Supplemental Methods for additional discussion). White shading represents extent of LGM glaciation (Gobejishvili et al., 2011) and black dashed line marks center of swath shown in Fig. 1. (B) Cosmogenic ^{10}Be erosion rates vs distance from the center of the swath (colored by mean elevation of sampled basins). Pearson's correlation coefficient (r) is shown comparing erosion rates and distance from the swath center, along with respective p value. (C) Cosmogenic ^{10}Be erosion rates vs distance along the swath (colored by distance from the swath center). Grey regions indicate estimated vertical component of uplift from the GC-LC convergence (Fig 1C) assuming convergence on a 2° or 45° dipping thrust. Correlation coefficient between E and GC-LC convergence (Fig 1C) is shown (see also Fig. S5). Average time is calculated as the amount of time required to erode 60 cm.

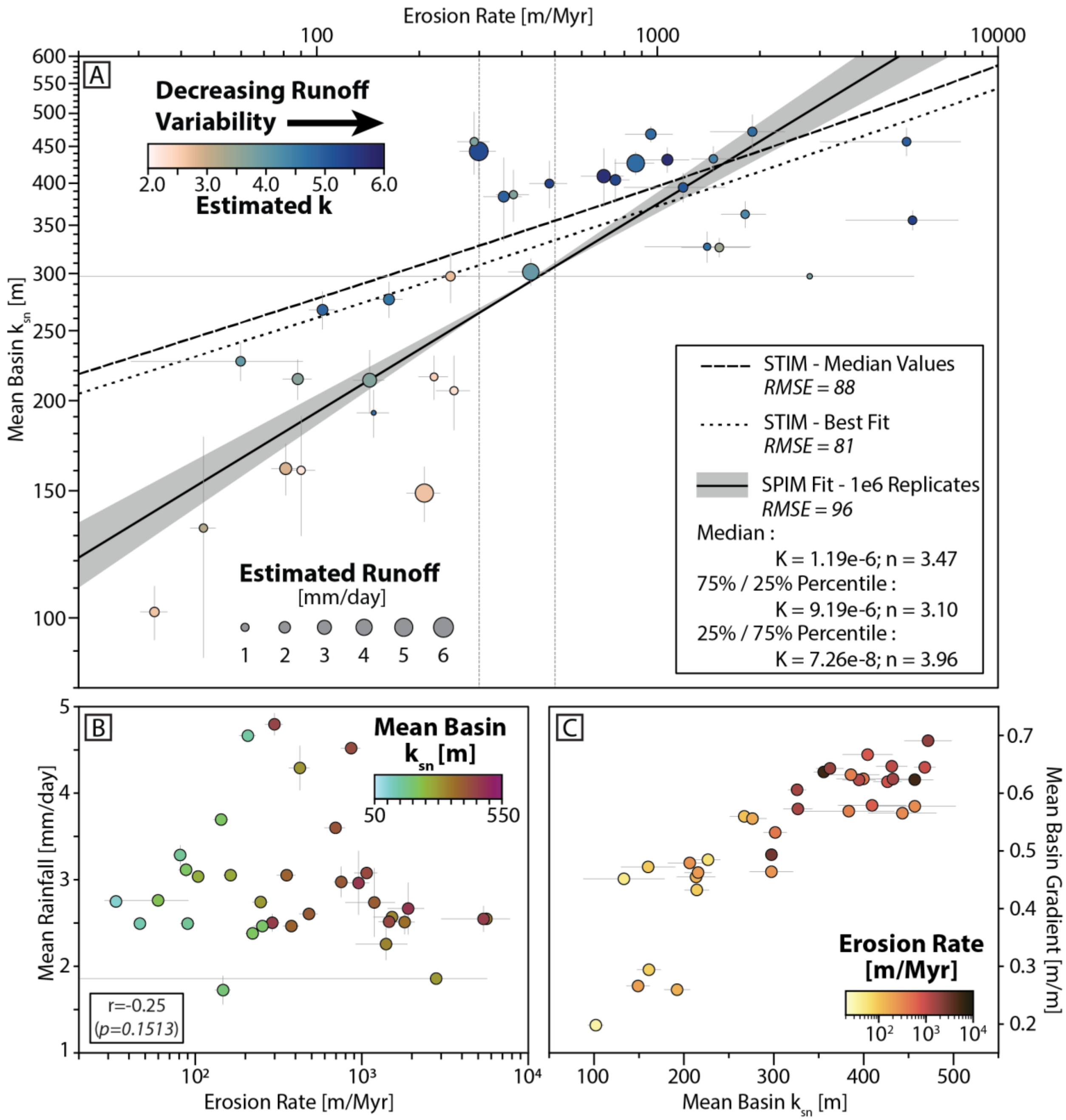

Fig. 8 (A) ^{10}Be erosion rate vs basin-averaged normalized channel steepness (k_{sn}). Individual basins are colored by estimated runoff variability and the size of the circles are scaled by estimated mean runoff. Curves represent best-fit power law function, stochastic threshold incision model using median values of k, R, and k_e, and a best-fit stochastic threshold incision model with free k, R, and k_e values from an ODR fit of the STIM equations. Vertical dashed lines highlight the range of E above which k_{sn} becomes largely invariant. Details of the power law fit are provided in Fig. S11. Residuals of the SPIM and STIM relations are presented in Fig. S16. (B) ^{10}Be erosion rate vs mean rainfall in each basin colored by k_{sn}. Pearson's correlation coefficient (r) between erosion rate and rainfall along with p-value is shown, note that this suggests

non-statistically significant correlation between these variables. (C) Mean basin k_{sn} compared to mean hillslope gradient, colored by E. Note that the linear relationship between k_{sn} and gradient reflects that both k_{sn} and gradient become insensitive to increases in erosion rate at ~500 m Myr^{-1} (Fig. S9).

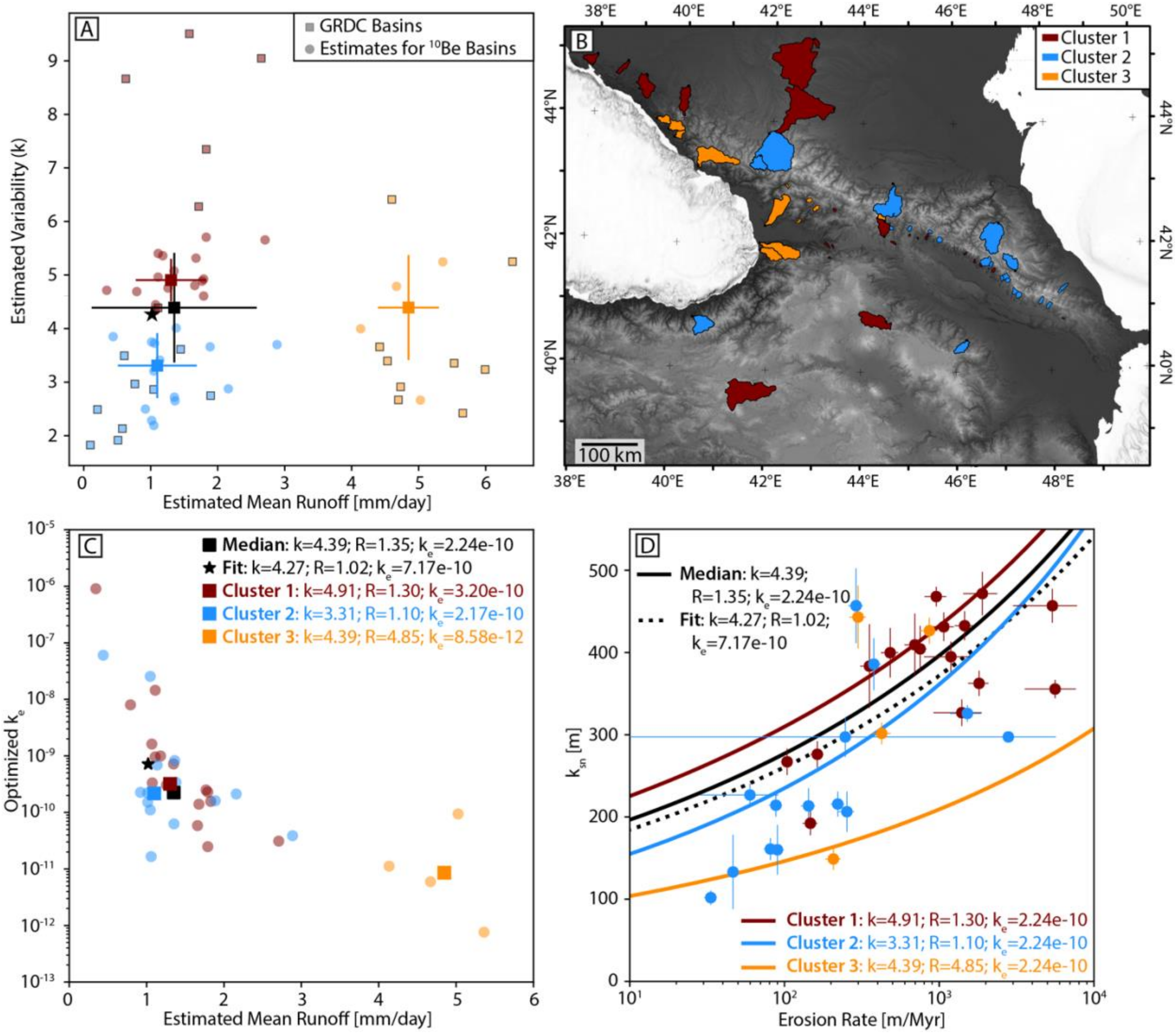

Fig. 9 (A) Result of k-means cluster analysis (3 clusters) using the estimated variability and mean runoff magnitudes as cluster variables. Cluster medians and standard deviations are shown with opaque square symbols and whiskers. Smaller transparent squares represent gauged GRDC basins. Black symbol represents whole population median and standard deviations. Black star is the best-fit variability and runoff from the STIM fit. (B) Both ^{10}Be and GRDC basins colored by cluster membership (analogous to Fig. 6B). (C) Estimated mean runoff vs. optimized k_e value with population medians shown as squares. Best-fit STIM k_e value shown with a star. (D) ^{10}Be erosion rates vs k_{sn} (analogous to Fig 8A). Basins are colored by their membership in clusters defined in A and B. Curves represent interpreted stochastic threshold incision model using median values from clusters. All curves except the fit use the population median k_e. Median and

fit lines are the same as in Fig. 8A. Additional details with respect to the cluster analysis are presented in Figs. S17-21.

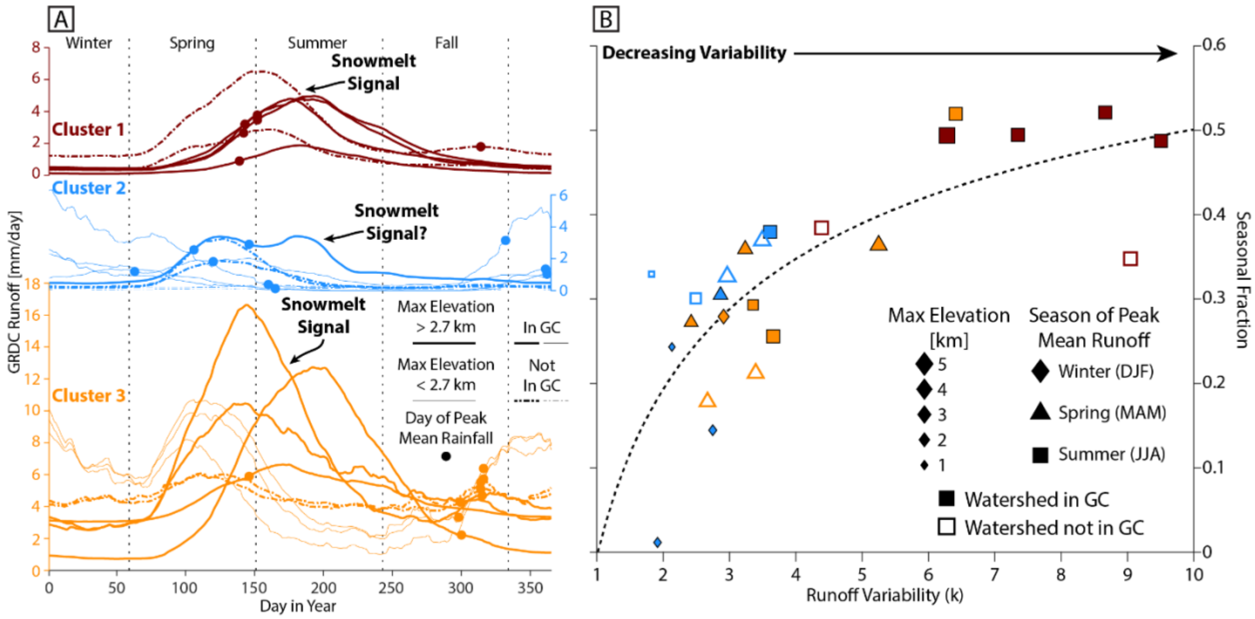

Fig 10. (A) Daily GRDC runoff, averaged over the full length of each dataset and after applying a 31-day moving average. Dots are day of peak rainfall from TRMM processed in the same way for the basin of interest. Note that y-axis positions for these dots do not indicate magnitude of the rainfall peak (see Supplementary Fig. 31 for rainfall time series). Runoff in high elevation basins of cluster 1 and 3 show a strong seasonality in runoff that is offset from timing of peak rainfall. Almost all basins show a peak in runoff in either the spring or summer consistent with derivation from snowmelt. (B) Seasonal fraction of runoff versus runoff variability for GRDC basins. Symbol size is scaled by maximum elevation, shapes indicate the season of maximum mean runoff, and colors indicate cluster membership. A power law fit through the data is shown to help visualize relationship and emphasizes that the GC basins (solid symbols) show a more consistent relationship than those further afield (open symbols).

References

Adams, B.A., Whipple, K.X., Forte, A.M., Heimsath, A.M., Hodges, K.V., 2020. Climate controls on erosion in tectonically active landscapes. Sci. Adv. 6. https://doi.org/10.1126/sciadv.aaz3166

Allen, M.B., Jackson, J., Walker, R., 2004. Late Cenozoic reorganization of the Arabia-Eurasia collision and the comparison of short-term and long-term deformation rates. Tectonics 23, doi:10.1029/2003TC001530-doi:10.1029/2003TC001530.

Anders, A.M., Roe, G.H., Montgomery, D.R., Hallet, B., 2008. Influence of precipitation phase on the form of mountain ranges. Geology 36, 479. https://doi.org/10.1130/G24821A.1

Avdeev, B., Niemi, N.A., 2011. Rapid Pliocene exhumation of the central Greater Caucasus constrained by low-temperature thermochronometry. Tectonics 30. https://doi.org/10.1029/2010TC002808

Balco, G., Stone, J., Lifton, N.A., Dunai, T., 2008. A complete and easily accessible means of calculating surface exposure ages or erosion rates from 10Be and 26Al measurements. Quat. Geochronol. 3, 174–195. https://doi.org/10.1016/j.quageo.2007.12.001

Berghuijs, W.R., Woods, R.A., Hutton, C.J., Sivapalan, M., 2016. Dominant flood generating mechanisms across the United States: Flood Mechanisms Across the U.S. Geophys. Res. Lett. 43, 4382–4390. https://doi.org/10.1002/2016GL068070

Bierman, P.R., Nichols, K.K., 2004. Rock to sediment - slope to sea with 10Be - rates of landscape change. Annu. Rev. Earth Planet. Sci. 32, 215–235.

Bookhagen, B., Burbank, D., 2006. Topography, relief, and TRMM-derived rainfall variations along the Himalaya. Geophys. Res. Lett. 33, L08405–L08405. https://doi.org/10.1029/2006GL026037

Campforts, B., Vanacker, V., Herman, F., Vanmaercke, M., Schwanghart, W., Tenorio, G.E., Willems, P., Govers, G., 2020. Parameterization of river incision models requires accounting for environmental heterogeneity: insights from the tropical Andes. Earth Surf. Dyn. 8, 447–470. https://doi.org/10.5194/esurf-8-447-2020

Cowgill, E., Forte, A.M., Niemi, N.A., Avdeev, B., Tye, A., Trexler, C.C., Javakishvirli, Z., Elashvili, M., Godoladze, T., 2016. Relict basin closure and crustal shortening budgets during continental collision: An example from Caucasus sediment provenance. Tectonics 35, 2918–2947. https://doi.org/10.1002/2016TC004295

Deal, E., Braun, J., Botter, G., 2018. Understanding the Role of Rainfall and Hydrology in Determining Fluvial Erosion Efficiency. J. Geophys. Res. Earth Surf. 123, 744–778. https://doi.org/10.1002/2017JF004393

DiBiase, R.A., Whipple, K.X., 2011. The influence of erosion thresholds and runoff variability on the relationships among topography, climate, and erosion rate. J. Geophys. Res. 116. https://doi.org/10.1029/2011JF002095

DiBiase, R.A., Whipple, K.X., Heimsath, A.M., Ouimet, W.B., 2010. Landscape form and millennial erosion rates in the San Gabriel Mountains, CA. Earth Planet. Sci. Lett. 289, 134–144.

Ferrier, K.L., Huppert, K.L., Perron, J.T., 2013. Climatic control of bedrock river incision. Nature 496, 206–209. https://doi.org/10.1038/nature11982

Fisher, G.B., Bookhagen, B., Amos, C.B., 2013. Channel planform geometry and slopes from freely available high-spatial resolution imagery and DEM fusion: Implications for channel width scalings, erosion proxies, and fluvial signatures in tectonically active landscapes. Geomorphology 194, 46–56. https://doi.org/10.1016/j.geomorph.2013.04.011

Forte, A.M., Cowgill, E., Murtuzayev, I., Kangarli, T., Stoica, M., 2013. Structual geometries and magnitude of shortening in the eastern Kura fold-thrust belt, Azerbaijan: Implications for the development of the Greater Caucasus Mountains. Tectonics 32. https://doi.org/10.1002/tect.20032

Forte, A.M., Cowgill, E., Whipple, K.X., 2014. Transition from a singly vergent to doubly vergent wedge in a young orogen: The Greater Caucasus. Tectonics 33, 2077–2101. https://doi.org/10.1002/2014TC003651

Forte, A.M., Whipple, K.X., 2019. Short communication : The Topographic Analysis Kit (TAK) for TopoToolbox. Earth Surf. Dyn. 7, 87–95. https://doi.org/10.5194/esurf-7-87-2019

Forte, A.M., Whipple, K.X., Bookhagen, B., Rossi, M.W., 2016. Decoupling of modern shortening rates, climate, and topography in the Caucasus. Earth Planet. Sci. Lett. 449, 282–294. https://doi.org/10.1016/j.epsl.2016.06.013

Forte, A.M., Whipple, K.X., Cowgill, E., 2015. Drainage network reveals patterns and history of active deformation in the eastern Greater Caucasus. Geosphere 11. https://doi.org/10.1130/GES01121.1

Gobejishvili, R., Lomidze, N., Tielidze, L., van der Meer, J.J.M., 2011. Late Pleistocene (Würmian) Glaciations of the Caucasus, in: Ehlers, J., Gibbard, P.L., Hughes, P.D. (Eds.), Quaternary Glaciations - Extent and Chronology. Elsevier, Amsterdam, pp. 141–147.

Harel, M.A., Mudd, S.M., Attal, M., 2016. Global analysis of the stream power law parameters based on worldwide 10Be denudation rates. Geomorphology 268, 184–196. https://doi.org/10.1016/j.geomorph.2016.05.035

Johnson, J.P.L., Whipple, K.X., Sklar, L., 2010. Contrasting bedrock incision rates from snowmelt and flash floods in the Henry Mountains, Utah. Geol. Soc. Am. Bull. 122, 1600–1615.

Kadirov, F., Floyd, M., Alizadeh, A., Guliev, I., Reilinger, R., Kuleli, S., King, R., Toksoz, M.N., 2012. Kinematics of the eastern Caucasus near Baku, Azerbaijan. Nat. Hazards 63, 997–1006.

Kirby, E., Whipple, K.X., 2012. Expression of active tectonics in erosional landscapes. J. Struct. Geol. 44, 54–75.

Klein Tank, A.M.G., Wijngaard, J.B., Können, G.P., Böhm, R., Demarée, G., Gocheva, A., Mileta, M., Pashiardis, S., Hejkrlik, L., Kern-Hansen, C., Heino, R., Bessemoulin, P., Müller-Westermeier, G., Tzanakou, M., Szalai, S., Pálsdóttir, T., Fitzgerald, D., Rubin, S., Capaldo, M., Maugeri, M., Leitass, A., Bukantis, A., Aberfeld, R., van Engelen, A.F.V., Forland, E., Mietus, M., Coelho, F., Mares, C., Razuvaev, V., Nieplova, E., Cegnar, T., Antonio López, J., Dahlström, B., Moberg, A., Kirchhofer, W., Ceylan, A., Pachaliuk, O., Alexander, L.V., Petrovic, P., 2002. Daily dataset of 20th-century surface air temperature and precipitation series for the European Climate Assessment: EUROPEAN TEMPERATURE AND PRECIPITATION SERIES. Int. J. Climatol. 22, 1441–1453. https://doi.org/10.1002/joc.773

Lague, D., 2014. The stream power river incision model: evidence, theory and beyond. Earth Surf. Process. Landf. 39, 38–61. https://doi.org/10.1002/esp.3462

Lague, D., Hovius, N., Davy, P., 2005. Discharge, discharge variability, and the bedrock channel profile. J. Geophys. Res. 110, F04006–F04006. https://doi.org/10.1029/2004JF000259

Mifsud, C., Fujioka, T., Fink, D., 2013. Extraction and purification of quartz in rock using hot phosphoric acid for in situ cosmogenic exposure dating. Nucl. Instrum. Methods Phys. Res. B 294, 203–207. https://doi.org/10.1016/j.nimb.2012.08.037

Molnar, P., Anderson, R.S., Kier, G., Rose, J., 2006. Relationships among probability distributions of stream discharges in floods, climate, bed load transport, and river

incision. J. Geophys. Res. 111, F02001–F02001. https://doi.org/10.1029/2005JF000310
Mosar, J., Kangarli, T., Bochud, M., Glasmacher, U.A., Rast, A., Brunet, M.-F., Sosson, M., 2010. Cenozoic-Recent tectonics and uplift in the Greater Caucasus: a perspective from Azerbaijan, in: Sosson, M., Kaymakci, N., Stephenson, R.A., Bergerat, F., Starostenko, V.I. (Eds.), Sedimentary Basin Tectonics from the Black Sea and Caucasus to the Arabian Platform. Geological Society, London, pp. 261–280.
Murphy, B.P., Johnson, J.P.L., Gasparini, N.M., Sklar, L.S., 2016. Chemical weathering as a mechanism for the climatic control of bedrock river incision. Nature 532, 223–227. https://doi.org/10.1038/nature17449
Portenga, E.W., Bierman, P.R., 2011. Understanding Earth's eroding surface with 10Be. GSA Today 21, 4–10. https://doi.org/10.1130/G111A.1
Reilinger, R., McClusky, S., Vernant, P., Lawrence, S., Ergintav, S., Cakmak, R., Ozener, H., Kadirov, F., Guliev, I., Stepanyan, R., Nadariya, M., Hahubia, G., Mahmoud, S., Sakr, K., ArRajehi, A., Paradissis, D., Al-Aydrus, A., Prilepin, M., Guseva, T., Evren, E., Dmitrotsa, A., Filikov, S.V., Gomez, F., Al-Ghazzi, R., Karam, G., 2006. GPS constraints on continental deformation in the Africa-Arabia-Eurasia continental collision zone and implications for the dynamics of plate interactions. J. Geophys. Res. 111, doi:10.1029/2005JB004051-doi:10.1029/2005JB004051.
Rossi, M.W., Anderson, R.S., Anderson, S.P., Tucker, G.E., 2020. Orographic Controls on Subdaily Rainfall Statistics and Flood Frequency in the Colorado Front Range, USA. Geophys. Res. Lett. 47. https://doi.org/10.1029/2019GL085086
Rossi, M.W., Whipple, K.X., Vivoni, E.R., 2016. Precipitation and evapotranspiration controls on event-scale runoff variability in the contiguous United States and Puerto Rico. J. Geophys. Res. 121. https://doi.org/10.1002/2015JF003446
Schaefli, B., Rinaldo, A., Botter, G., 2013. Analytic probability distributions for snow-dominated streamflow: Snow-Dominated Streamflow Pdfs. Water Resour. Res. 49, 2701–2713. https://doi.org/10.1002/wrcr.20234
Scherler, D., Bookhagen, B., Strecker, M.R., 2014. Tectonic control on 10 Be-derived erosion rates in the Garhwal. J. Geophys. Res. Earth Surf. 119, 83–105. https://doi.org/10.1002/2013JF002955
Scherler, D., DiBiase, R.A., Fisher, G.B., Avouac, J.-P., 2017. Testing monsoonal controls on bedrock river incision in the Himalaya and Eastern Tibet with a stochastic-threshold stream power model. J. Geophys. Res. Earth Surf. 122, 1389–1429. https://doi.org/10.1002/2016JF004011
Schwanghart, W., Scherler, D., 2014. Short Communication: TopoToolbox 2 - MATLAB based software for topographic analysis and modeling in Earth surface sciences. Earth Surf. Dyn. 2, 1–7. https://doi.org/10.5194/esurf-2-1-2014
Sklar, L., Dietrich, W.E., 2006. The role of sediment in controlling steady-state bedrock channel slope: Implications of the saltation-abrasion incision model. Geomorphology 82, 58–83.
Sokhadze, G., Floyd, M., Godoladze, T., King, R., Cowgill, E.S., Javakhishvili, Z., Hahubia, G., Reilinger, R., 2018. Active convergence between the Lesser and Greater Caucasus in Georgia: Constraints on the tectonic evolution of the

Lesser–Greater Caucasus continental collision. Earth Planet. Sci. Lett. 481, 154–161. https://doi.org/10.1016/j.epsl.2017.10.007

Stone, J.O., 2000. Air pressure and cosmogenic isotope production. J. Geophys. Res. Solid Earth 105, 23753–23759. https://doi.org/10.1029/2000JB900181

Trexler, C.C., Cowgill, E., Spencer, J.Q.G., Godoladze, T., 2020. Rate of active shortening across the southern thrust front of the Greater Caucasus in western Georgia from kinematic modeling of folded river terraces above a listric thrust. Earth Planet. Sci. Lett. 544, 116362. https://doi.org/10.1016/j.epsl.2020.116362

Tucker, G.E., 2004. Drainage basin sensitivity to tectonic and climatic forcing: Implications of a stochastic model for the role of entrainment and erosion thresholds. Earth Surf. Process. Landf. 29, 185–204. https://doi.org/10.1002/esp.1020

Vezzoli, G., Garzanti, E., Limonta, M., Radeff, G., 2020. Focused erosion at the core of the Greater Caucasus: Sediment generation and dispersal from Mt. Elbrus to the Caspian Sea. Earth-Sci. Rev. 200, 102987. https://doi.org/10.1016/j.earscirev.2019.102987

Vincent, S.J., Carter, A., Lavrishchev, A., Rice, S.P., Barabadze, T.G., Hovius, N., 2011. The exhumation of the western Greater Caucasus: a thermochronometric study. Geol. Mag. 148, 1–21. https://doi.org/10.1017/S0016756810000257

Vincent, S.J., Somin, M.L., Carter, A., Vezzoli, G., Fox, M., Vautravers, B., 2020. Testing Models of Cenozoic Exhumation in the Western Greater Caucasus. Tectonics 39. https://doi.org/10.1029/2018TC005451

Whipple, K.X., 2009. The influence of climate on the tectonic evolution of mountain belts. Nat. Geosci. 2, 97–104.

Whipple, K.X., Meade, B., 2004. Controls on the strength of coupling among climate, erosion, and deformation in two-sided, frictional orogenic wedges at steady state. J. Geophys. Res. 109, F01011–F01011. https://doi.org/10.1029/2003JF000019